Cathodoluminescence studies of GaN coalesced from nanopyramids selectively grown by MOVPE

K J Lethy[1], P R Edwards[1], C Liu[2], P. Shields[2], D Allsopp[2] and R W Martin[1],

1Department of Physics, SUPA, Strathclyde University, Glasgow, G4 0NG

2Department of Electronic and Electrical Engineering, University of Bath, BA2 7AY

Email: lethy.kj@strath.ac.uk

Abstract

Coalescence of GaN over arrays of GaN nanopyramids has important device applications and has been achieved on nano-imprint lithographically patterned GaN/sapphire substrates using metal organic vapour phase epitaxy. Spatially and spectrally resolved cathdoluminescence (CL) from such coalesced layers are studied in detail. The observed red shift of the GaN band edge emission with increasing electron beam depth of maximum CL into the coalesced layer is discussed in relation to a carrier induced peak shift, likely due to Si out-diffusion from the mask material into the GaN. Depth resolved CL measurements are used to quantify the red shift in terms of band-gap renormalization and strain effects. CL maps showing the GaN near band edge peak energy distribution reveal micron-scale domain-like variations in peak energy and are attributed to the effects of local strain.

GaN-based light emitting diodes (LEDs) and laser diodes (LDs) in the UV/blue/green wavelength range are necessary for applications like full colour displays, solid state lighting, short-haul optical communications, back lights for liquid crystal displays, laser printers and read-write laser sources for high density information storage [1,2]. For the realisation of GaN-based next generation opto-electronic devices with improved optical power, quantum efficiency and operating lifetime, reductions in threading dislocation density (TDD) are essential. The conventional technique of epitaxial lateral overgrowth (ELO) can reduce TDDs in GaN-on-sapphire to ~ 10^6 cm^{-2} [3, 4]. This micron-scale ELO technique has attracted extensive attention since Nakamura *et al.* demonstrated blue laser diodes with lifetimes exceeding 10,000 hours on ELO GaN in the 1990s [4, 5]. Theoretical and experimental studies show that further reductions in the TDD are possible if the ELO technique is extended to the nanoscale, which will be referred to as nano-ELO (NELO) [6,7]. Moreover, the NELO process can overcome limitations such as the processing of efficient devices only above the ELO wings and the need for very thick ELO GaN layers (of the order of tens of microns) in order to achieve significant reduction of TDDs.

Zang *et al.* [8] have reported dislocation densities down to 10^8 cm^{-2} for a 2.5 μm thick NELO GaN layer grown over a nanopatterned SiO_2 mask, deposited on a Si substrate by metal organic vapour phase epitaxy (MOVPE). Wang *et al* [9] reported a TDD as low as ~ 10^7 cm^{-2} for a 4 μm NELO GaN layer grown over a nanoporous SiO_2 mask. A high light extraction efficiency as well as dislocation reduction for NELO GaN grown over a SiO_2 nanorod array formed on a sapphire substrate has been reported by Chiu *et al* [10]. These reports indicate that the surface of NELO GaN has fewer defects in contrast to ELO where threading dislocations originating from the interface in the window regions propagate to the surface. However, most publications on the subject focus on the TDDs and include only brief details on the analysis of the optical properties of the nano-ELO GaN.

Here we report an investigation of optical properties of a series of NELO GaN layers using high spatial and spectral resolution cathodoluminescence (CL) spectroscopy. This CL set up combines aspects of both spectroscopy and microscopy and allows fast mapping of regions of the

NELO layers, providing visualisation of the internal microstructure and information on the local luminescence [11]. The CL maps and spectra are subsequently used to provide details of the residual strain variation across the coalesced GaN layers.

The GaN layers were grown by MOVPE in an Aixtron AIX 200/4HT RF-S reactor, using both conventional and pulsed growth modes. A nanopatterned growth mask was fabricated from 100 nm SiO_2 by nanoimprint lithography (NIL) on n-doped GaN templates (~$4x10^{18}cm^{-3}$) grown on c-plane sapphire substrates (typical dislocation density $1x10^9$ cm^{-2}). The nanopatterns are hexagonal arrays of circular pores with a diameter of about 200 nm and a pitch of about 450 nm, giving a pattern fill-factor of ~ 50 %. In the conventional growth mode, gallium (group III) and nitrogen (group V) precursors are switched into the growth chamber simultaneously, whereas in pulsed growth mode the group V sources are intermittently supplied while the group III sources are supplied continuously. Pulsed mode MOVPE enhances the migration length of the group III species and promotes lateral growth [12, 13]. The results described here were obtained from three typical samples. Samples A and B are grown with 40 pulses to give a thickness of approximately 300 nm for the coalesced GaN layer, whilst twice as many pulses were used for sample C to give a thicker coalesced layer (~ 700 nm) of GaN. Growth of samples B and C included interruptions during the pulsed growth conditions, with a short (2 minute) period of normal growth at raised temperature occurring after every 10 pulse cycles. More details on sample growth are given in Ref. [12]. The light emitting properties of the samples were studied by room temperature CL hyperspectral imaging using two different set ups: a field emission SEM using an angled sample [11] and an electron probe micro-analyser [14] respectively.

Figure 1(a) shows a representative cross-sectional secondary electron (SE) image of sample B. The cross-sectional images together with large area SE images of partially coalesced regions (not shown), indicate that the initial GaN deposition forms nanopyramids in the window regions [15]. The subsequent changes in the growth conditions favour the lateral growth and coalescence of these nanopyramids over the SiO_2 mask (dark regions in Fig 1(a)), giving the formation of a thick continuous GaN layer [10]. Figures 1(b) and 1(d) show planar SE images of

samples A, B and C. The surface of sample C is seen to have higher density of surface features than the others, with the presence of many closed loop like features having dark contrast and extending over the surface.

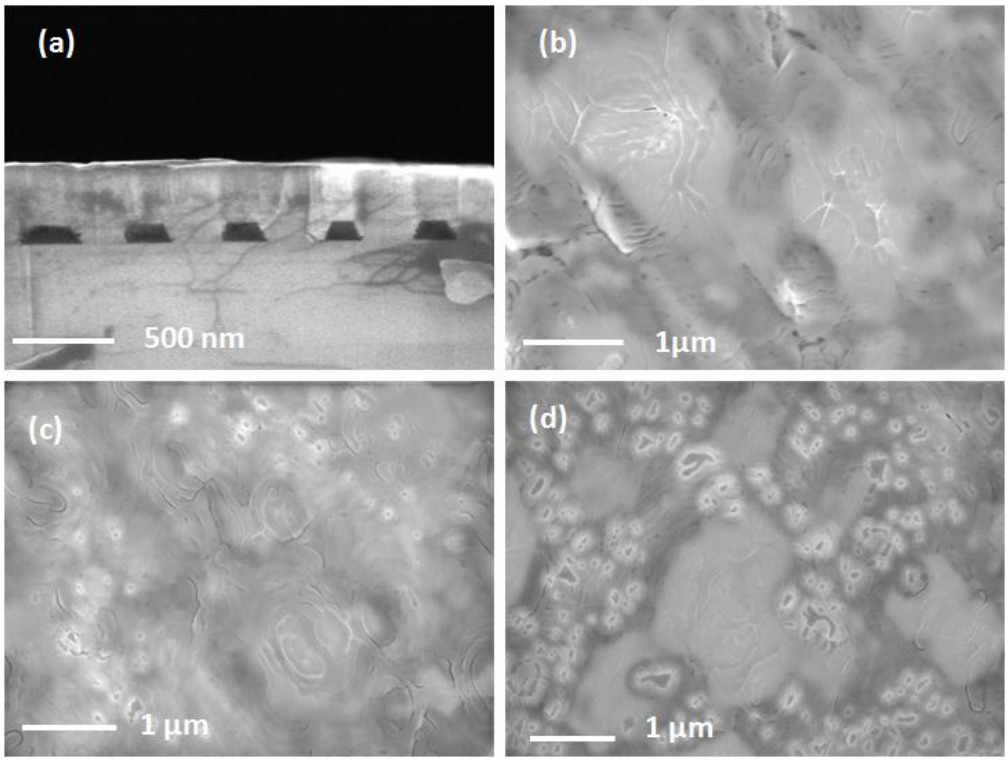

Fig 1. (a) Cross-sectional SEM image for sample B, and SEM images of coalesced layer of GaN for samples (b) A, (c) B and (d) C. The dark trapezoidal like boxes appearing in Fig.1 (a) are SiO_2 mask material.

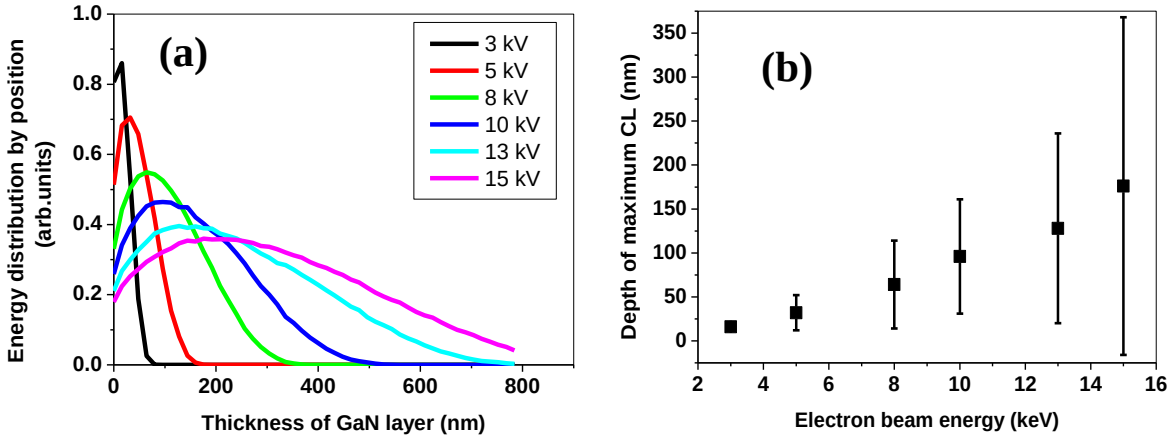

Fig. 2(a) Electron beam energy deposition estimated using Monte-Carlo Simulation of the electron trajectories in a thick GaN layer (b) depth of maximum CL vs electron beam acceleration voltage with the error bars representing the range within which 85 % of the maximum electron beam energy loss occurs within the GaN epilayers.

The NELO process can be regarded as a layered process that involves first forming nanopyramids and then promoting lateral growth followed by conventional growth [12]. As such, depth resolved characterisation techniques can provide valuable information about factors that influence the properties of coalesced epitaxial films. Depth resolved CL spectra (in plan-view mode) from the samples are obtained by exciting the samples with different electron beam acceleration voltages varying from 3 to 15 kV. The electron beam energy deposition profile in a thick GaN epilayer is shown in Figure 2 (a) as a function of electron beam energy. The peak of the electron beam energy distribution profile, for each electron beam energy shown in Figure 2(a) corresponds to the maximum electron beam energy loss within the GaN epilayer and can be associated with the formation of the maximum number of e-h pairs and hence the depth at which maximum CL signal generation occurs [16]. The depth corresponding to this maximum electron beam energy loss will be used for the depth scale in this report. Figure 2(b) shows the depths for the maximum CL emission as a function of beam acceleration voltage. The error bars represent the depth range within which 85 % of the maximum energy loss of the incident exciting electron beam occurs. The increase in size of these error bars with increase in acceleration voltage is commensurate with the broad nature of the electron energy loss profile [Fig 2(a)] within the GaN epilayer at higher electron beam voltages.

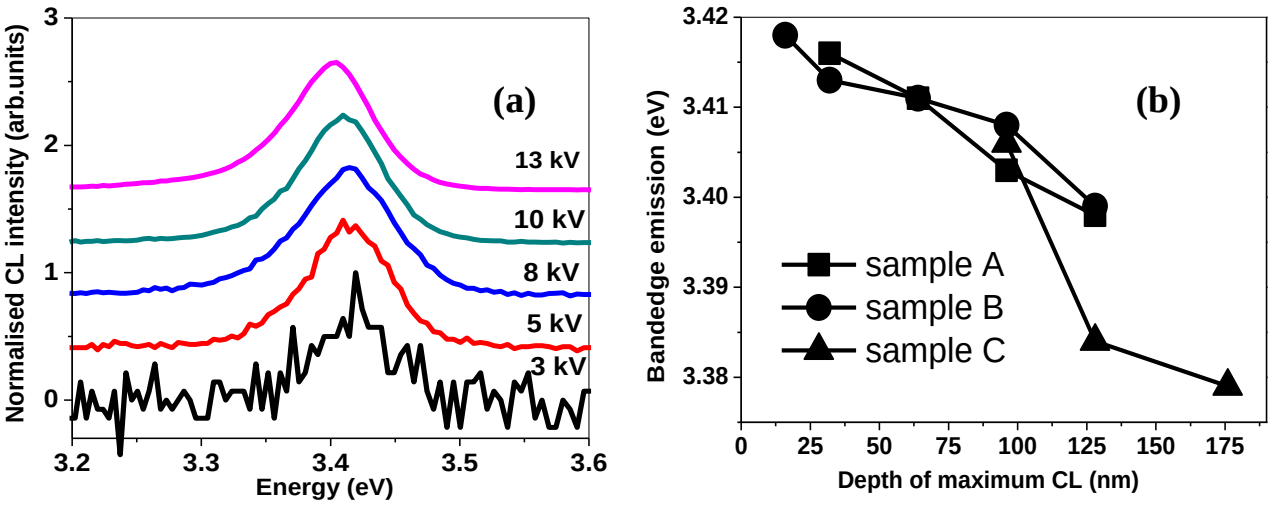

Fig 3. (a) CL spectra as a function of electron beam voltage for Sample B. (b) Peak emission energy vs depth of maximum CL for all three samples.

Table 1. CL line width and intensity for different samples at 10 keV electron beam energy

Sample	Line width (meV)	CL Intensity (counts)
A	82	540
B	81	590
C	89	140

Depth resolved CL spectra from sample B are shown in figure 3(a), revealing a red-shift of the GaN near band edge (NBE) emission peak with increasing electron beam penetration. The peak positions of the GaN peaks are fitted using Gaussian functions and plotted as a function of the depth of maximum CL for all three samples in figure 3(b). As the depth of maximum CL increases, the peak energy is observed to red shift from the bandgap energy for bulk unstrained wurtzite GaN (3.42 eV) [17]. It might be supposed that this indicates a reduction in tensile stress within the GaN layers towards their top surface, but later in this paper we will show that energy shifts due to doping must also be considered. With sample C it was necessary to excite with a higher voltage electron beam (corresponding to greater depth) to generate a CL signal. The SE images in figure 1 indicate that sample C has a higher density of surface features, which may be causing a higher rate of non-radiative recombination in its near-surface layer. However, despite

the lower radiative efficiency of the sub-surface layer in sample C it is notable that all three samples show a very similar shift of peak energy with depth within the sample. Our previous results on such NELO GaN layers have shown a non-radiative defect density of ~ 1-3 x 10^8 cm^{-2} and much lower locally [18]. A similar defect concentration can be expected for the present samples, though their precise density is sensitive to the precise coalescence process involved. A comparison of the CL emission intensity and line width for all the samples is shown in Table 1 for electron beam energy of 10 keV. The maximum luminescence intensity and minimum line width are obtained for sample B, suggesting that this layer has the best crystal quality. The interpretation of the excitation energy dependent CL is confirmed by measurement of CL spectra from a cross-section of sample B (figure 4 (a) and (b)). The CL peak measured from below the mask region (position a) is red-shifted, by approximately 18 meV, compared to that from the coalesced region (positions b and c). It is noteworthy that the CL peak emission wavelength and FWHM are both very similar for the wing and seed regions. This observation is in contrast to the GaN NBE behaviour in micron-scale patterned lateral epitaxial growth, where the peak energy and FWHM of GaN NBE emission from wing and seed region differ [19]. Monte-Carlo simulations show that at 5 kV the CL comes from a volume approximately 120 nm in diameter, which limits the ability to compare intensities for the cross-sectional CL spectra from the different regions.

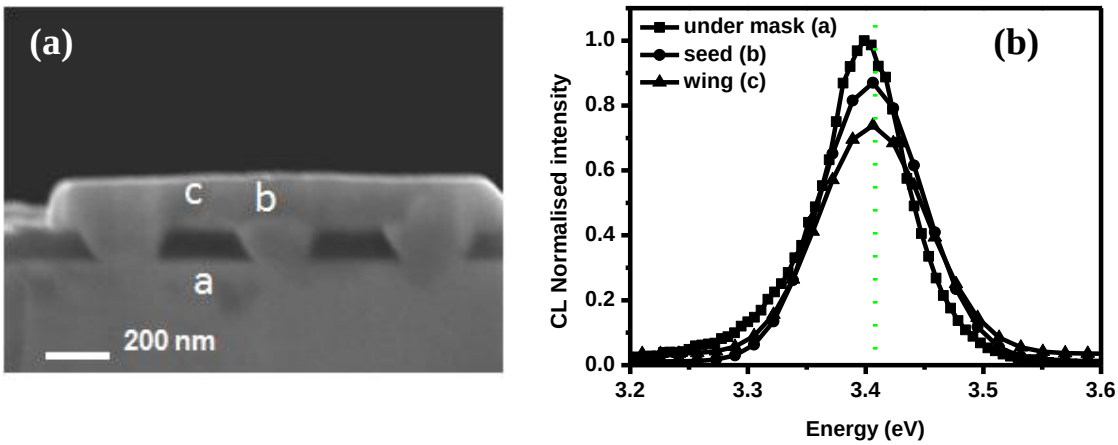

Fig. 4(a) Cross-sectional SEM and (b) RT CL spectra for sample B excited using a 5 keV electron beam. The vertical dashed line marks the peak of the CL for the wing region.

The values of the NBE exciton energies are known to depend on the built-in strain within the GaN layer which when grown on a sapphire substrate is generally under in-plane compressive strain. Although the stress due to the lattice mismatch between GaN and sapphire can be relaxed at a film thickness of less than several nanometers, a significant compressive strain builds up in the GaN layer during cool down from the growth temperature due to the difference in the coefficients of thermal expansion between the GaN and sapphire. As the film thickness increases the residual compressive strain in the GaN layer will decrease if dislocations form [20]. This compressive strain blueshifts the NBE energy compared to the value for bulk GaN, and this shift is expected to increase with depth in a GaN-on-sapphire sample. The network of dislocations usually exists in the first few nm of the coalesced epilayer [12]. Whilst the dislocations help to relieve the compressive stress in the lower level of the coalesced layer, there is evidence that the epitaxy grown between the nanopyramids in the early stage of coalescence can be under compressive strain [21]. Therefore, *a priori* assumptions about strain relaxation near the interface with the growth mask contributing to the observed red shift cannot be made. Detailed analysis of the possible causes of the red shift must be performed. The observed red shift in band edge emission peak with increasing depth of maximum CL in the samples in this study is therefore unexpected. In addition to strain, the effect of possible changes in doping levels on emission peak energies should be considered. Unintentional n-type doping of GaN structures grown through ELO mask windows and the dependence of dopant concentration on different growth facets have previously been reported for micron-scale ELOG GaN [22]. Similar effects can be expected in the nano-scale variant described here resulting in a non-uniformly n-type doped GaN coalesced layer, although the scale is naturally much smaller, such effects will be revealed through the lateral and/or vertical localised variation in GaN NBE CL peak energy as discussed in this paper. Possible causes are discussed below.

To obtain spatially resolved luminescence information across the coalesced layers hyperspectral CL maps are acquired for all samples, using different electron beam energies to provide information as a function of depth. These hyperspectral CL maps, composed of 100 × 100

pixels are acquired from 20 × 20 μm areas using a scan step size of 200 nm. Figure 5(b) shows the integrated intensity CL map for the coalesced layer from sample C obtained for an electron beam voltage of 15 kV. The mapped region is shown in the white box on the secondary electron image [figure 5(a)] and the intensity map reveals regions of contrast of micron scale size. The bright spots have diameters of 2-5 μm, which are likely to correspond to the size of relatively defect free regions in the coalesced layer.

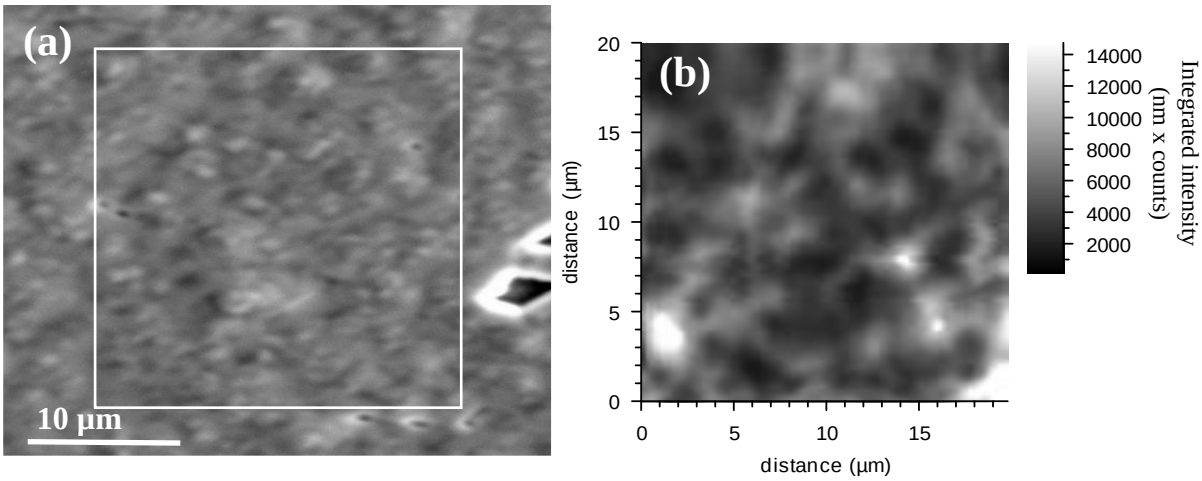

Fig 5 (a) Secondary electron image of the coalesced layer for sample C, (b) integrated intensity CL map of the coalesced layer shown in the white box in (a).

The spatially averaged CL spectra collected from the mapped region show a single peak similar to those in figure 3(a) and Gaussian peak fitting using a non-linear least squares algorithm is used to generate maps showing the distribution of the peak height, centre energy and FWHM for GaN NBE. Figure 6 shows depth resolved centre energy CL maps for sample A (8 kV and 10 kV) and a 13 kV map for sample C. The depth of maximum CL in GaN for electron beam energies of 8, 10 and 13 keV are approximately 60, 100 and 130 nm, respectively, ensuring the excitation volume is confined, or nearly confined, within the coalesced GaN layers of the respective samples. Moreover, the depth range within which the maximum number of e-h pair formation occurs within the GaN epilayers as shown in Figure 2 (b) must also be considered. The CL maps reveal two types of variation in peak energy ranging from 3.37 to 3.41 eV. The first occurs on a distance

corresponding to ~1-3 periods (450 nm) of the growth mask pattern. These can be related to strain variations and/or unintentional doping in and between neighbouring GaN nanopyramids [12]. However, data shown below indicate that the contribution to the lateral variation in GaN NBE emission energy due to doping variations is relatively small. The second type of lateral variation in the CL emission peak occurs on a scale of ~2-4 μm and may originate from the microstructure within the template below the mask region [23]. No significant variation in domain size with depth is observed for samples A and B. The corresponding integrated CL intensity maps (not shown) also show micron-scale random variations due to the random distribution of defects. It is worth noting that the FWHM maps corresponding to the GaN NBE emission show a variation of only 3-6 meV across the mapped 20 x 20 μm area of the coalesced layer, with an example shown in figure 6(d).

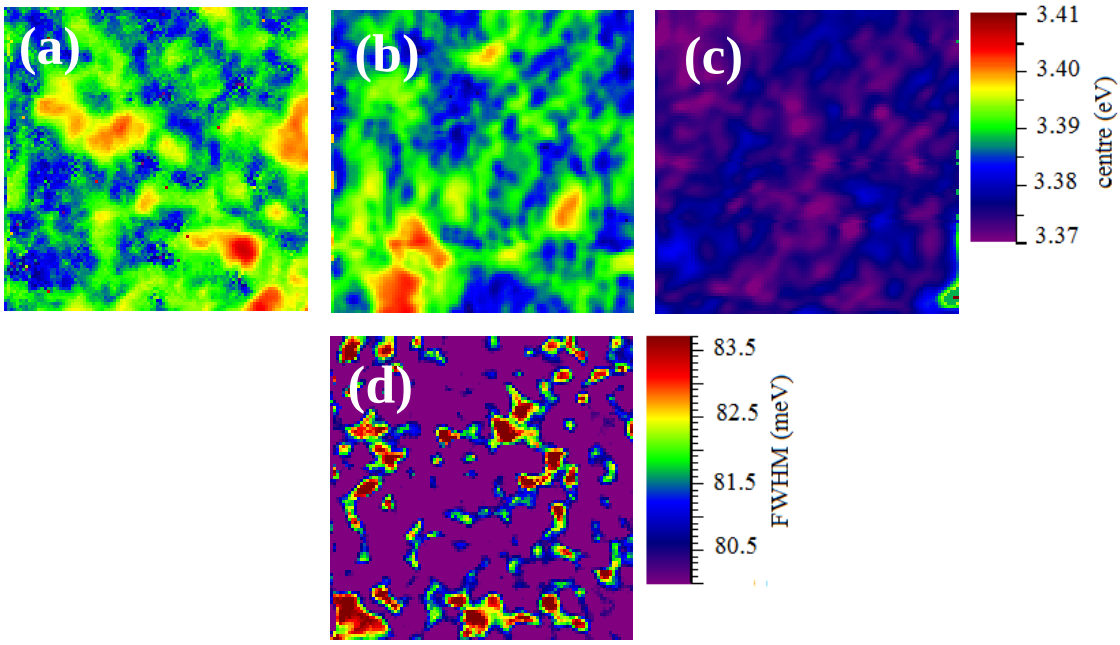

Fig.6 Curve fitted centre energy maps of the GaN band edge CL emission at RT for the samples A (at 8 and 10 kV) and C (10 kV) for (a), (b) and (c) respectively. To make the energy shift clearer the same energy scales are used. (d) CL map showing the FWHM distribution for sample A for 10 keV electron beam energy. All images are 20 x 20 μm.

To study the effect of individual nanoholes in the selective growth mask on the luminescence properties, higher spatial resolution hyperspectral CL maps were acquired from

sample A. The CL intensity map (acquired using an 8 kV electron beam) for the band edge emission shows a hexagonal pattern (figure 7(a)), which likely corresponds to the hexagonal symmetry of the nanohole lattice arrangement. To correlate the features in this map with the underlying mask, a SE image of a different region of the nanostructured sample, where the coalescence was incomplete, is compared to the band edge intensity map. The alignment indicates that the intensity of the band edge emission is relatively higher for the regions of coalesced GaN above the growth mask compared to that from the regions located in the growth windows. Enhanced emission intensity from the regions above the growth mask would correlate with an improved crystal quality of GaN in the laterally overgrown wing regions along with an intensity enhancement due to reflection of backward travelling light at the interface of the GaN and buried SiO_2 layer.

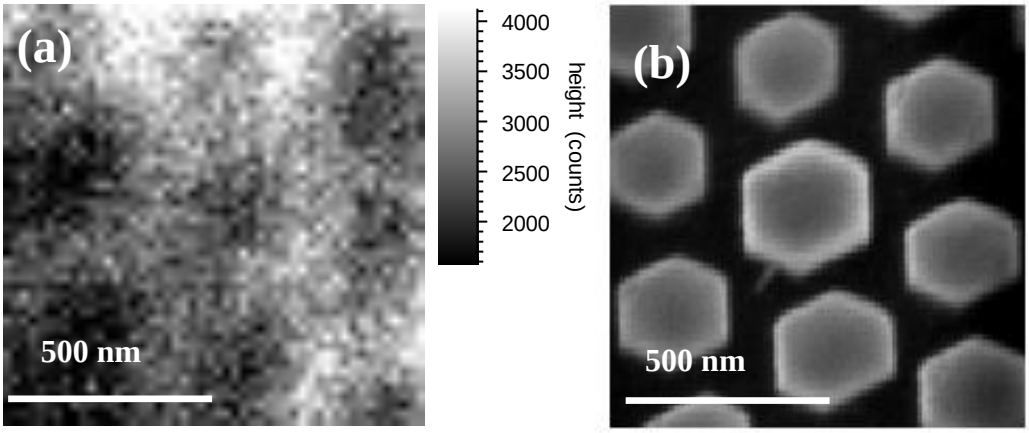

Fig 7(a) Band edge CL emission intensity map for the sample A acquired using an 8 kV electron beam in a FESEM. (b) Secondary electron image from a different region of the nanopyramid array where the coalescence is incomplete,

In addition to the effect of built-in-strain, the band edge emission peaks are affected by temperature, carrier concentration and the energy of the incident electron beam. The influence of the latter on the band edge emission peak can have two origins; one related to the penetration depth of the electron beam in the coalesced layer, which increases with beam energy, and second an excitation power induced peak shift. Since low injection conditions are maintained for the CL

mapping, the effect of excitation power on band edge emission peak position is expected to be negligible in comparison to penetration depth effects. With increase in depth from the sample surface, the possible factors contributing to strain variation are: (1) lattice and thermal expansion coefficient mismatch between the substrate and GaN, resulting in a residual compressive strain, (2) tensile strain due to the presence of Si, and (3) any stress arising due to coalescence effects. The presence of high concentrations of silicon and oxygen (acting as n-type dopants), possibly from the SiO_2 mask and/or the n-GaN template, can influence both strain and carrier concentration in a GaN lattice and can contribute to a red shift of the NBE emission through bandgap renormalization (BGR). This is a reduction in the fundamental bandgap energy caused by doping densities in excess of about 10^{18} cm^{-3} within GaN [24, 25]. Another direct effect of Si doping in GaN is the broadening of the PL/CL line width of the near band edge emission [24, 26].

Substitution of Si in place of Ga in the GaN lattice might also be expected to lead to tensile strain and a net contraction of the lattice as the Si atoms (~ 100 pm) are smaller than the Ga atoms (130 pm). Dadger et al [27] and Lee et al [28] have previously observed tensile strain in Si doped GaN layers. However, according to Romano et al [29], the tensile stress due to Si doping is not related to the change in lattice constant of GaN rather it is due to an increase in surface roughness (which increases with decrease in effective crystallite size) and crystallite coalescence. Since our nanopyramids (which coalesce to form the GaN epilayers) are of ~ 200 nm, size-related effects could be significant. Based on these considerations the observed shift in band edge emission peak (ΔE) can be treated as a sum of the shifts due to strain, including that induced by Si, (ΔE_{strain}) and to the carrier concentration induced by the Si donors ($\Delta E_{carrier}$):

$$\Delta E = E_{CL} - E_{bulk} = \Delta E_{strain} + \Delta E_{carrier} \qquad [1]$$

Hence, estimation of $\Delta E_{carrier}$ enables an estimation of the strain induced GaN peak shift in the coalesced layers.

The carrier concentration in these layers can be estimated using data for the PL FWHM of Si-doped GaN published by Yoshikawa et al. [30] , Lee et al. [24] and Schubert *et al.* [31]. The following power law dependence is generated by combining the FWHM and Si concentration data in these three reports:

$$FWHM\,(meV) = 49 + 8.4\times10^{-12} n^{2/3} \qquad [2]$$

where n is the carrier density. This expression does not include any strain dependence of the GaN CL line width, which is expected to be very small [26, 32]. This is supported by the CL maps of these samples, where the GaN FWHM varies by only ~ 3 meV whilst the corresponding peak energy shifts by about 30-35 meV [figures 6(a) and 6(d)] and also from the FWHM comparison of the cross-sectional spot CL spectra collected from the wing and seed region [figure 4(b)].

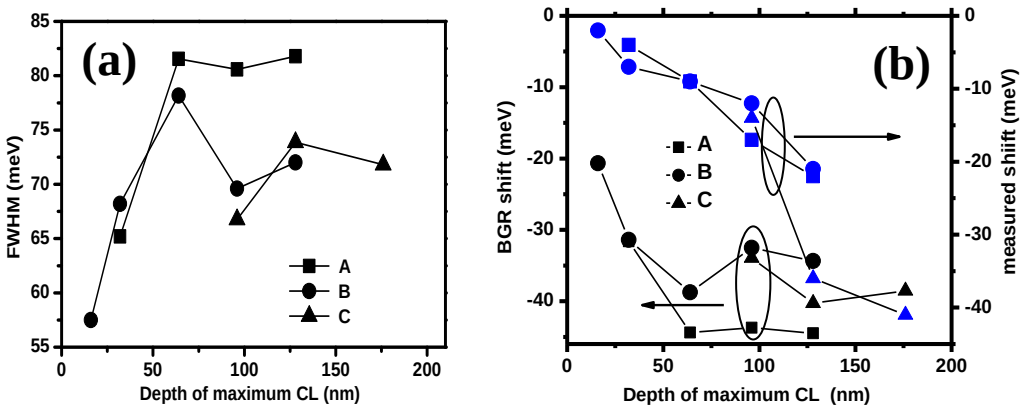

Fig. 8(a) Room temperature band edge CL line width (b) bandgap narrowing shift and measured shift vs depth of maximum CL for the three samples

Figure 8(a) shows the variation of the FWHM estimated from the CL spectra for the three samples as a function of depth of maximum CL. The much reduced variation in FWHM for Fig. 6(d) in comparison to Fig. 8(a), showing lateral and vertical respectively, suggests a marginal influence of any lateral doping gradient on the variation of GaN NBE emission energy. Also there is no systematic variation with lateral in either the GaN NBE CL peak energy or its FWHM

(Fig 6) which can be expected in facet dependent impurity incorporation. This may possibly imply that in nanoscale heteroepitaxy, the n-type dopants are more or less uniformly distributed across a coalesced layer due to the nanoscale patterning. This is further supported by the nearly similar values of FWHM for the CL spectra collected from the wing and seed region [Figure 4b]. Equation 2 is used to estimate carrier concentrations from the FWHMs in Fig. 8, giving values varying from 9.6×10^{17} to 7.6×10^{18} cm^{-3}. From this analysis the carrier densities increase with the depth of maximum CL up to a depth of about of 70 nm (corresponding to an electron beam voltage of ~ 8 kV). When the depth range of CL excitation is considered, the 85 % range in Figure 2(b), it is seen that this corresponds to the region of excitation approaching the SiO_2 mask. Beyond this the carrier densities reach a plateau. These carrier concentrations are sufficient to shift the GaN bandgap energy via BGR. The bandgap reduction due to BGR can be estimated using the following relation [22],

$$\Delta E_{carrier} = Kn^{1/3} \qquad [3]$$

where K is the BGR coefficient and n the carrier density. Lee *et al* [24] have reported BGR coefficients of -1.38×10^{-8} and -2.1×10^{-8} eV cm for moderately and heavily compensated Si doped GaN layers, respectively. Based on the estimates of the Si doping density in the coalesced layers in the region just above the growth mask, the BGR coefficients for samples A, B and C are calculated to be -2.27, -2.05 and -2.31×10^{-8} eV cm, respectively. Figure 8 (b) shows the BGR red shift in band edge CL peak position due to the raised carrier concentrations and the measured red shift ΔE (from figure 2(b)) as a function of depth. In all samples the shifts reach values close to, or exceeding, 40 meV as the excited region reaches depths close to the SiO_2 masks. Thus bandgap renormalization will account for a large proportion of the observed red shift. Moreover, a comparison of the measured shift and BGR shift reveals that at each depth of maximum CL, the corresponding biaxial strain shift (ΔE_{strain} in Equation 1) in bandgap energy should be positive;

implying the prevailing compressive strain at each depth from the sample surface. The obtained BGR red shift values are comparable to the values reported previously for Si doped GaN [24, 30]

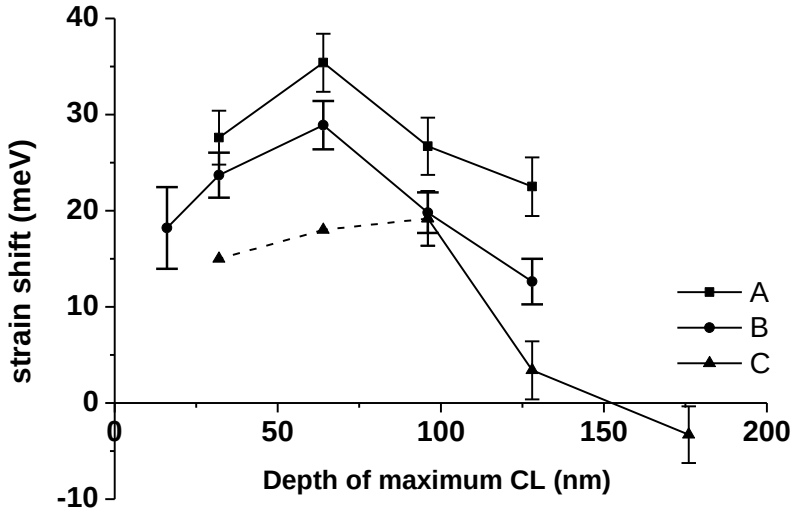

Fig 9 Biaxial strain shifts for the three samples as a function of electron beam penetration depth. The dashed line extends the plot for sample C to the two simulated data points, as described in the text.

These BGR shift values are then used to quantify the CL band edge emission peak shift due to biaxial strain by subtracting the estimated BGR shifts from the total shift. The resulting shifts due to biaxial strain are plotted in figure 9. The error bars for the strain shift are estimated by considering the uncertainties in the values for FWHM and peak positions as well as the uncertainties for the coefficients in equation 2 and 3. For the thinner samples there is a peak in the strain induced shift at the excitation energy that corresponds to the depth of maximum CL reaching down to the buried mask, when the 85 % is taken into account. The positive strain shifts, corresponding to compressive strain, decrease for lower penetration depths giving the expected strain relaxation towards the surface. Further, the observed positive strain shifts imply that the residual compressive strain dominates the tensile strain due to the presence of Si. For sample C, which has the thickest coalesced layer, measurements at low beam accelerating voltage (i.e for low beam penetration depths) could not be made. However, in order to allow some tentative comparison with the thinner samples the trend in measured $E_{CL} - E_{bulk}$ with depth of maximum

CL has been extrapolated to lower depths for this sample. Two simulated data points are then added to Figure 9 and marked by the dashed line. The predicted strain shift with depth into the coalesced layer is quantitatively similar to that found for samples A and B, apart from the peak in the compressive strain appearing somewhat further below the free surface, and is also of approximately the same magnitude.

Conclusion

Nanoscale epitaxial lateral overgrowth of GaN has been carried out on a GaN sapphire template by MOVPE using nanopatterned SiO_2 as the mask material. The room temperature depth-resolved CL band edge emission spectra from coalesced GaN layers are red shifted from the bandgap energy for bulk unstrained GaN. The red shifts have been analysed in terms of contributions from a depth dependent compressive strain in the coalesced layer and band gap renormalisation arising from unintentional Si doping originating from the growth mask. From the variations in the FWHM of the CL peak a contribution from BGR was calculated for each sample and was found to be a maximum at or near the interface with the growth mask, a result consistent with Si out-diffusion from the latter. Further, the likely contribution of variations in the compressive stress in the coalesced GaN layer with depth could be deduced. It was found for all three samples that, starting from the interface with the growth mask, the compressive strain increases, peaks and then falls again at the free surface. The peak in the compressive strain occurs at approximately the same depth, ~50-100 nm below the free surface, although this is likely to vary from sample to sample depending on factors like the coalescence layer thickness and the density of threading dislocations. Finally, the lateral spatially resolved maps reveal micron-scale domain-scale variations possibly reflecting the microstructure of the GaN template below the growth mask.

References

1. Khan A, Balakrishnan K, and Katona T 2008 *Nature Photonics* **2** 77
2. Nakamura S 2009 *Mater. Res. Bull*. **34** 101
3. Zheleva T S, Nam O-H, Bremser M D, and Davis R F 1997 *Appl. Phys.Lett.* **71** 2472
4. Nakamura S, Senoh M, Nagahama S, Iwasa N, Yamada T, Matsushita T, Kiyoku H, Sugimoto Y, Kozaki T, Umemoto H, Sano M, and Chocho K 1998 *Appl. Phys. Lett.* **72** 211
5. Nakamura S, Senoh M, Nagahama S, Iwasa N, T. Yamada T, Matsushita T, Kiyoku H, Sugimoto Y, Kozaki T, Umemoto H, Sano M, and Chocho K 1998 *J. Cryst. Growth* **189/190** 820
6. Alizadeh A, Sharma P, Ganti S, LeBoeuf S F and Tsakalakos L 2004 *J. Appl. Phys.* **95** 8199
7. Tsakalakos L, Alizadeh A, Huber W, Malenfant P, Stein J, Seker F, Reitz J, Ganti S and Sharma P 2004 *Methods of defect reduction in wide bandgap thin films using nanolithography, US20040077156*
8. Zang K Y and Chua S J 2008 *Phys Status Solidi C* **5** 1585
9. Wang Y D, Zang K Y, Chua S J, Tripathy S, Zhou H L and Fonstad C G, 2006 *Appl. Phys. Lett*. **88** 211908
10. Chiu C H et al 2008 *Appl. Phys. Lett*. **93** 081108
11. Edwards P R and Martin R W 2011 *Semicond.Sci.Technol.* 26 064005
12. Liu C, Shields P A, Chen Q, Allsopp D W E, Wang W N, Bowen CR, Phan T L and Cherns D 2010 *Phys. Status Solidi C* **7** 32
13. Ren D W, Zhou W and Dapkus P D 2005 *Appl. Phys.Lett.* **86** 111901
14. Martin R W, Edwards P R, O'Donnell K P, Dawson M D, Jeon C W, Liu C, Rice G R and Watson I M 2004 *Phys. Status Solidi A* **201** 665
15. Liu C, Satka A, Lethy K J, Edwards P R, Allsopp D, Martin R W, Shields P, Kovac J, Uherek F and Wang W 2009 *Appl. Phys. Exp.* **2** 121002
16. Hovington P, Drouin D and Gauvin R 1997 *Scanning* **19** 1
17. Lee W S 2009 *Appl. Phys. Lett.* **94** 082105
18. Shields P et al 2011 *Phys.Status. Solidi (c)* **8** 2334
19. Roskowski A M, Preble E A, Einfeldt S, Miraglia P M, and Davis R F 2002 *IEEE J. Quantum Electronics* **38** 1006
20. Kim C, Robinson I K, Myoung J, Shim K, Cheol Yoo M and Kim K 1996 *Appl. Phys. Lett.* **69** 2358
21. Satka A, Shields P and Allsopp D W E (Article in press)
22. Sumner J, Oliver R A, Kappers M J and Humphreys C J 2009 *J.Appl.Phys.* **106** 104503
23. Shields P A, Liu C, Šatka A, Trampert A, Zúñiga-Pérez J, Alloing B, Haško D, Uherek F, Wang W, Causa F and Allsopp D 2011 *Phys. Status Solidi C* **8** 2334
24. Lee I H, Lee J J, Kung P, Sanchez F J and Razeghi M 1999 *Appl. Phys. Lett.* **74** 102
25. Chine Z, Rebey A, Touati H, Goovaerts E, Oueslati M, El Jani B and Laugt S 2006 *Phys. Status Solidi A* **203** 1954

26. Koh E K, Woo Park I, Choi H, Yoon M, Choh S H, Kim H S, Cho Y M, Kim S and Park S S 2005 *J. of Crystal Growth* **276** 37
27. Dadgar A, Schulze F, Zettler T, Haberland K, Clos R, Straßburger G, Bläsing J, Diez A and Krost A 2004 *J. Cryst. Growth* **272** 72
28. Lee I H, Choi I H, Lee C R, Shin E, Kim D, Noh S K, Son S J, Lim K Y, and Lee H J 1998 *J. Appl. Phys.* **83** 5787
29. Romano L T, Van de Walle C G, Ager J W, Götz W and Kern R S 2000 *J. Appl. Phys.* **87** 7745
30. Yoshikawa M, Kunzer M, Wagner J, Obloh H, Schlotter P, Schmidt R, Herres N, and Kaufmann U 1999 *J. Appl. Phys.* **86** 4400
31. Schubert E F, Goepfert I D, and Grieshaber W 1997 *Appl. Phys. Lett.* **71** 921
32. Kudrawiec R, Rudziski M, Serafinczuk J, Zajc M and Misiewicz J 2009 *J. Appl. Phys.* **105** 093541